

Local variations in defect polarization and covalent bonding in ferroelectric Cu^{2+} -doped PZT and KNN functional ceramics at the morphotropic phase boundary†

Rüdiger-A. Eichel,^{*a} Ebru Erünal,^a Michael D. Drahus,^a Donald M. Smyth,^b Johan van Tol,^c Jérôme Acker,^d Hans Kungl^d and Michael J. Hoffmann^d

Received 20th March 2009, Accepted 18th June 2009

First published as an Advance Article on the web 28th July 2009

DOI: 10.1039/b905642d

Cu^{2+} -doped $\text{Pb}[\text{Zr}_{0.54}\text{Ti}_{0.46}]\text{O}_3$ (PZT) and Cu^{2+} -doped $[\text{K}_{0.5}\text{Na}_{0.5}]\text{NbO}_3$ (KNN) ferroelectrics with a dopant concentration of 0.25 mol% were investigated by means of multi-frequency and multi-pulse electron paramagnetic resonance (EPR) spectroscopy. Through the use of high magnetic fields and pulsed microwave fields an enhanced resolution was achieved yielding valuable information about the structural distortion at the dopant site. The results obtained suggest that Cu^{2+} substitutes for both systems as an acceptor centre for the perovskite B-site. For reasons of local charge compensation, different kinds of defect associates invoking one and two oxygen vacancies are formed. These two kinds of extended defects differ in their electric and elastic properties. The results obtained are analyzed in order to characterize differences of the local structure in the Cu^{2+} -defect center for morphotropic phase boundary compositions between the two systems. In particular, it is found that Cu^{2+} -doping in KNN creates 50% more oxygen vacancies than the same amount of copper in PZT. Furthermore, local differences in covalent and ionic bonding are monitored.

Introduction

Functional ceramics based on lead zirconate titanate solid solutions ($\text{Pb}[\text{Zr}_x\text{Ti}_{1-x}]\text{O}_3$, PZT) provide a basis for a wide range of applications.^{1–4} Principally there are two strategies for tailoring material properties for specific applications. On the one-hand, the Zr/Ti-ratio may be varied, where compositions at the so-termed *morphotropic phase boundary* (MPB) typically show optimum values. On the other hand, material properties may be tailored by adding several transition-metal or rare-earth elements on a percentage level. This allows control of the defect structure,^{5–7} which is typically achieved by means of aliovalent doping, rendering ‘soft’ or ‘hard’ piezoelectric materials.⁸ Even though PZT is the material-of-choice for the majority of ferro- and piezoelectric devices, there is a strong interest in developing lead-free alternatives to PZT owing to environmental concerns. As suggested by the knowledge obtained from PZT, the candidate material should be a solid-solution system having an MPB. One of the most

promising candidates are potassium sodium niobates ($[\text{K}_y\text{Na}_{1-y}]\text{NbO}_3$, KNN).^{9–11}

The pseudo-binary PZT solid-solution system as a function of temperature is divided into a cubic paraelectric (P_c) and a ferroelectric phase (*cf.* Fig. 1(a)). As a function of composition, the region of ferroelectric phase is divided by a MPB into two parts: a tetragonal phase region on the Ti-rich side (F_t) and a rhombohedral phase region on the Zr-rich side ($F_{r1,2}$). On the other hand, the KNN phase diagram consists of several low-temperature ferroelectric phases ranging from tetragonal

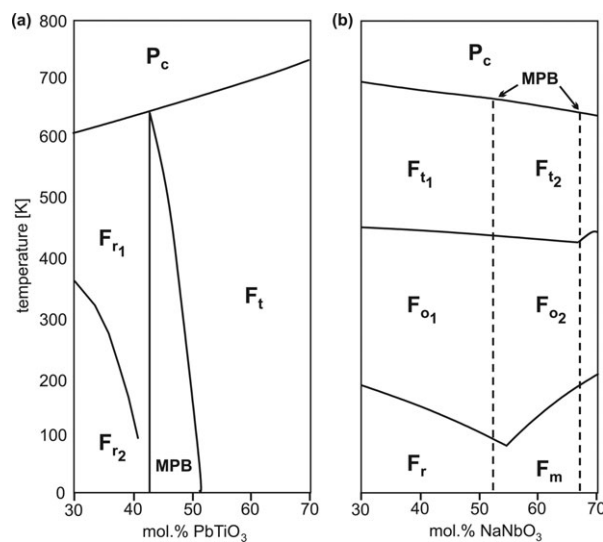


Fig. 1 Phase diagrams for the $\text{Pb}[\text{Zr}_x\text{Ti}_{1-x}]\text{O}_3$ (a) and $[\text{K}_y\text{Na}_{1-y}]\text{NbO}_3$ (b) solid solution systems indicating the regions of the morphotropic phase boundary.

^a Institut für Physikalische Chemie I, Universität Freiburg, Albertstr. 21, D-79104 Freiburg, Germany.

E-mail: ruediger.eichel@physchem.uni-freiburg.de;

Fax: +49 (0)761 2036222

^b Materials Research Center, Lehigh University, Bethlehem, PA 18015, U.S.A.

^c Center for Interdisciplinary Magnetic Resonance, National High Magnetic Field Laboratory, Florida State University, Tallahassee, Florida 32310, USA

^d Institute of Ceramics in Mechanical Engineering, University of Karlsruhe, D-76131 Karlsruhe, Germany

† This article was submitted as part of a Themed Issue on electron paramagnetic resonance. Other papers on this topic can be found in issue 31 of vol. 11 (2009). This issue can be found from the PCCP homepage [http://www.rsc.org/pccp].

($F_{1,2}$) over orthorhombic ($F_{o1,2}$) to rhombohedral (F_r) and monoclinic (F_m), as illustrated in Fig. 1(b). Even though for both PZT and KNN the MPB occurs for $x \approx 0.5$ (cf. Fig. 1), there is a fundamental different structure of the MPB. For PZT the MPB connects the rhombohedral phase, in which the electric polarization is along the [111] direction, to the tetragonal structure, in which the polarization lies along the [001] direction, necessitating a ‘rotation of polarization’. On the other hand, for KNN there is no such necessity as the MPB connects regions of collinear directions of spontaneous polarization. Because for PZT it is suggested that the extraordinarily large piezoelectric response in the MPB region is driven by the electric-field induced rotation of the electric polarization,^{12–14} the exact role of the MPB for KNN materials is currently controversial.^{11,15,16}

On a microscopic level, two main questions for piezoelectric compounds are of concern: a closer understanding of the nature of the MPB and the interplay between structural features of the MPB with the defect structure. In this paper we thus aim to compare two specific structural features between PZT and KNN; the formation of defect associates through doping with aliovalent copper ions and the role of the corresponding defect-dipole polarization at the MPB.

Concerning the defect structure it has to be distinguished between so-called ‘hard’ materials with relatively low dielectric constants or high coercive fields, and ‘soft’ compounds that show an increased dielectric constant, high dielectric loss or low coercive field. For PZT it is well established that acceptor-type dopants form defect dipoles with charge-compensating oxygen vacancies, such as $(\text{Cu}_{\text{Ti}}'' - V_{\text{O}}^{\bullet\bullet})^{\times}$,¹⁷ $(\text{Ni}_{\text{Ti}}'' - V_{\text{O}}^{\bullet\bullet})^{\times}$,^{18,19} $(\text{Fe}_{\text{Zr,Ti}} - V_{\text{O}}^{\bullet\bullet})^{\bullet 20-26}$ or $(\text{Mn}_{\text{Ti}}'' - V_{\text{O}}^{\bullet\bullet})^{\times}$.²⁷ The KNN defect structure is more complex. Recently, beyond the existence of $(\text{Cu}_{\text{Nb}}''' - V_{\text{O}}^{\bullet\bullet})'$ defect dipoles, the formation of a second type of defect associate $(V_{\text{O}}^{\bullet\bullet} - \text{Cu}_{\text{Nb}}''' - V_{\text{O}}^{\bullet\bullet})^{\bullet}$ with predominant elastic properties has been found.²⁸ On the other hand, donor-type functional centers for PZT rather occur as ‘isolated’ centers ($\text{Gd}_{\text{Pb}}^{\bullet}$) and the corresponding lead vacancies (V_{Pb}'') generated for charge compensation are located in distant coordination spheres.²⁹

The *method-of-choice* to characterize paramagnetic dopants is provided by electron paramagnetic resonance (EPR) spectroscopy.^{5,6} Because it is a local-probe technique, it is particularly well suited for an investigation of the MPB. Recent methodological advances concerning the use of high frequencies^{30–33} and pulsed microwave fields^{17,34,35} have allowed for an accurate determination of spin-Hamiltonian parameters. These in turn are able to be transferred into structural information through the use of semi-empirical methods,^{20,21,25,26,36} where density-functional theoretic (DFT) calculations have proved to be very helpful.^{17,25,37}

Theory

The spin Hamiltonian for an unpaired $3d^p$ electron with spin $S = \frac{1}{2}$ interacting with N magnetic active nuclei of arbitrary spin I can be written as³⁸

$$\mathcal{H} = \beta_e \mathbf{B}_0 \cdot \mathbf{g} \cdot \mathbf{S} - \beta_n \sum_{i=1}^N g_{n,i} \mathbf{B}_0 \cdot \mathbf{I}_i + \sum_{i=1}^N \mathbf{S} \cdot \mathbf{A}_i \cdot \mathbf{I}_i \quad (1)$$

where $g_{n,i}$ are the corresponding nuclear g -factors and β_e , β_n are the Bohr and nuclear magnetons, respectively. The first and second terms are the electronic and nuclear Zeeman interactions, respectively, where \mathbf{B}_0 denotes the external magnetic field. The last term corresponds to the hyperfine interactions with nearby magnetic nuclei, such as the copper hyperfine interaction with $I^{\text{Cu}} = \frac{3}{2}$ for both copper isotopes with natural abundances ^{63}Cu : 69.09% and ^{65}Cu : 30.91% and 100% abundant ^{23}Na ($I = \frac{3}{2}$) or 22.1% abundant ^{207}Pb ($I = \frac{1}{2}$) nuclei.³⁹ The hyperfine tensors \mathbf{A}_i as well as the external field \mathbf{B}_0 are given in the principal axes system of the g -matrix, and the index i refers to a particular nucleus. The copper nuclear quadrupole interaction was not resolved in the spectra and thus has been neglected.

The hyperfine interactions \mathbf{A}_i may then be expressed as

$$\mathbf{A}_i = a_{\text{iso},i} \mathbf{1} + \mathbf{A}'_i \quad (2)$$

where $a_{\text{iso},i}$ is the isotropic hyperfine coupling constant and the traceless and symmetric tensor \mathbf{A}'_i describes the anisotropic dipole–dipole interaction between the electron spin S and the nuclear spin I_i . Because the second-rank tensor \mathbf{A}'_i is traceless and symmetric, there is always a coordinate system in which the tensor is diagonal with the elements A'_\perp and $A'_\parallel = -2A'_\perp$. By convention, A'_\parallel is taken to be the principal value with the largest absolute magnitude. Therefore, the dipolar hyperfine interaction can be described in terms of this single parameter.

For an $S = \frac{1}{2}$, $I = \frac{1}{2}$ spin system with isotropic g -value and an axial hyperfine tensor, the nuclear transition frequencies in the two m_S manifolds are given by

$$\nu_{\alpha,\beta} = \left[\left(\frac{A}{2} \pm \nu_I \right)^2 + \left(\frac{B}{2} \right)^2 \right]^{\frac{1}{2}} \quad (3)$$

with the nuclear Zeeman frequency $\nu_I = -\frac{g_n \beta_n B_0}{h}$ and

$$\begin{aligned} A &= A_\parallel \cos^2 \theta + A_\perp \sin^2 \theta \\ &= a_{\text{iso}} + A'_\parallel (3 \cos^2 \theta - 1) \end{aligned} \quad (4)$$

$$\begin{aligned} B &= (A_\parallel - A_\perp) \sin \theta \cos \theta \\ &= 3A'_\parallel \sin \theta \cos \theta \end{aligned} \quad (5)$$

where θ is the angle between the vector \mathbf{r} joining the electron spin and the nucleus, and the A principal axes. Assuming a point-dipole approximation, the dipolar hyperfine parameter A'_\parallel scales as r^{-3}

$$A'_\parallel = \frac{\mu_0 g g_n \beta_e \beta_n}{4\pi r^3 h} \quad (6)$$

and hence provides an estimate for the distance between the paramagnetic center and the corresponding magnetic nucleus. This approximation is applicable only if hyperfine interaction with nuclei are considered, which are sufficiently remote from the localized electron spin. A vanishing trace of \mathbf{A} indicates the validity of this assumption.

Experimental

X-Band (9.4 GHz) continuous-wave and pulsed EPR measurements were performed on a Bruker ElexSys 680 spectrometer, using a cylindrical TE₀₁₁ dielectric ring resonator (Bruker). The exact magnetic field values were calibrated by a standard field marker (polycrystalline DPPH with $g = 2.0036$). All spectra were recorded at a temperature of 10 K, using a helium-flow cryostat (Oxford).

Field-modulated continuous wave EPR experiments at high-frequencies (240 GHz) were performed at the high magnetic field facility at the NHMFL, using a quartz synthesizer for the microwave (mw) radiation and a setup without resonator.⁴⁰

HYSCORE⁴¹ spectra were recorded using a standard four-pulse sequence ($\frac{\pi}{2} - \tau - \frac{\pi}{2} - t_1 - \pi - t_2 - \frac{\pi}{2} - \tau - \text{echo}$) and an eight-step phase cycle in order to remove unwanted echoes.⁴² Pulse lengths of $t_{\pi} = t_{\pi/2} = 16$ ns and a delay time of $\tau = 150$ ns were employed. The echo is recorded in two dimensions as a function of t_1 and t_2 , which were incremented independently from each other in steps of 8 ns, starting with initial values of 100 ns. Typically 512 data points were collected in both dimensions. The recorded time-domain data were then processed as follows: the background echo decay in both t_1 and t_2 dimension was removed by least-squares fitting to a third-order polynomial and subsequent subtraction. Both dimensions of the data were then zero filled to 1024 data points, convoluted with a Hamming window function and two-dimensional Fourier transformed, giving the frequency-domain HYSCORE spectrum. The spectra presented in this paper are contour plots with logarithmic scaling after magnitude calculation. These appear in two quadrants, referred to as the positive (+, +) and negative (+, -) quadrants.

The chemical composition of the materials is expected to be $\text{Pb}[\text{Zr}_{0.5387}\text{Ti}_{0.4588}\text{Cu}_{0.0025}]\text{O}_{2.9975}$ and $[\text{K}_{0.5}\text{Na}_{0.5}][\text{Nb}_{0.9975}\text{Cu}_{0.0025}]\text{O}_{2.99625}$, respectively.

Results

Multi-frequency EPR

Starting with the Cu^{2+} -functional center in PZT, the corresponding X-band (9.4 GHz) EPR spectrum is shown in Fig. 2(a). Although it is characteristic for a Cu^{2+} charge state, the spectral resolution is not sufficient to reliably extract a full set of spin-Hamiltonian parameters (*cf.* eqn (1)). In particular, the situation is complicated by the expected existence of several overlapping structures. On basis of the observed X-band spectrum it is even not possible to determine the number or site symmetry of such overlapping Cu^{2+} -species.

In order to enhance spectral resolution, an EPR spectrum at higher Larmor frequency (240 GHz) was taken (*cf.* Fig. 3).³³ At higher external fields, the Zeeman interaction becomes the dominant term in the spin Hamiltonian (1), thus simplifying the spectrum and facilitating the determination of the full g -matrices for the different Cu^{2+} -species. The corresponding spectrum exhibits the spectral shape expected for axial and rhombic g -matrices. Through numerical spectrum simulation⁴³ and subsequent least-squares fitting, one center of axial site symmetry ($g_{\perp}^{(1)} = 2.082$) and two different centers

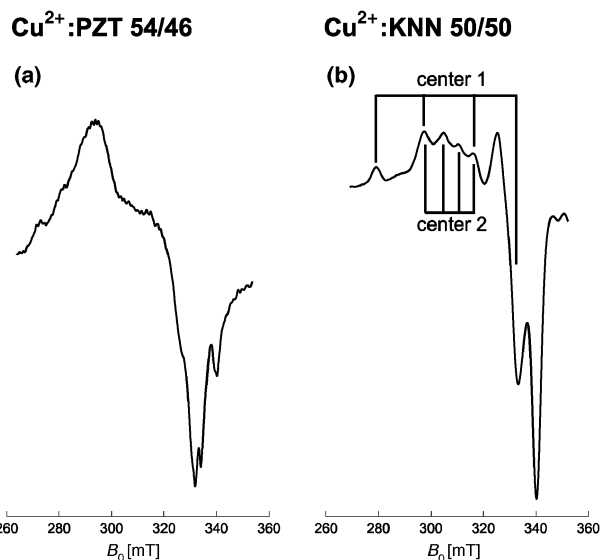


Fig. 2 X-Band (9.4 GHz) EPR-spectra at 10 K. (a) -0.25 mol% doped Cu:PZT 54/46. (b) -0.25 mol% doped Cu:KNN 50/50.²⁸ Stick spectra for the two different copper centers are indicated.

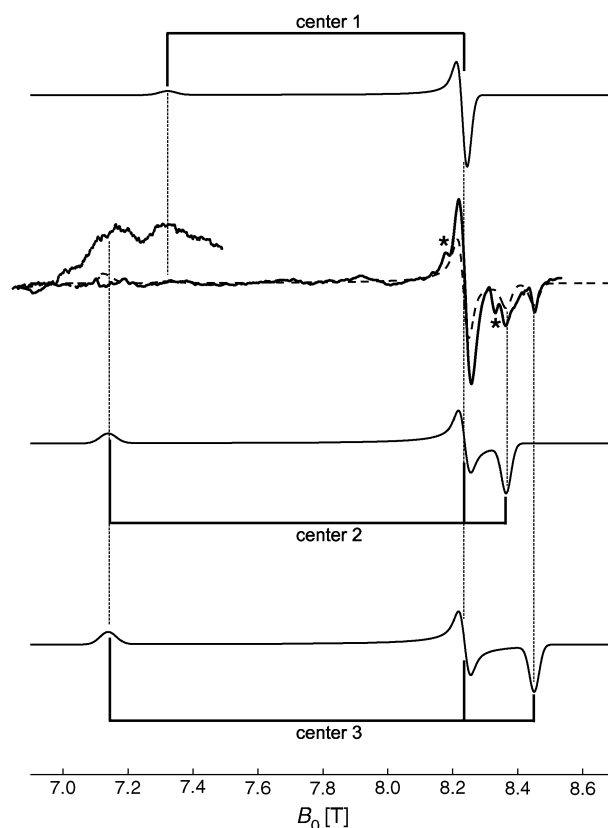


Fig. 3 High-field 240 GHz EPR-spectrum of 0.25 mol%-doped Cu:PZT 54/46 at 4 K.³³ The inset displays the low-field region recorded with increased signal-to-noise. Least-squares fit of the experimental 240 GHz EPR spectrum invoking three simulated copper spectra, one of axial and two of rhombic symmetry.

of rhombic symmetry ($g_{xx}^{(2)} = 2.050$, $g_{xx}^{(3)} = 2.029$) with identical $g_{yy}^{(2,3)} = 2.082$ are obtained. The corresponding set of (simulated) spectra is superimposed to the experimental

spectrum in Fig. 3. At the low-field edge of the spectrum at least two spectral features could be resolved (inset in Fig. 3). Because no *a priori* assignment of these features to particular axial and rhombic g -matrix components is possible, the relationship $g_{\parallel}^{(l)} < g_{zz}^{(r)}$ is assumed. This assignment is supported by the fact that the g_{\parallel} - and g_{zz} -values generally are sensitive to a change in covalency of the $\text{Cu}^{2+}\text{-O}^{2-}$ -in-plane π -bonding,^{36,37} which in turn is due to the $\text{Zr}^{4+}\text{-O}^{2-}$ -bonding being more polar (ionic) than the $\text{Ti}^{4+}\text{-O}^{2-}$ -bonding because of electro-negativity differences. Consequently, $g_{\parallel}^{(l)} = 2.342$ and $g_{zz}^{(r1)} = g_{zz}^{(r2)} = 2.402$. The two remaining resonances marked by an asterisk are assigned to Fe^{3+} -impurity centers.³³ The copper hyperfine interaction was not resolved in the spectra and at high fields primarily leads to line broadening, constraining any further analysis.

Compared to PZT, the Cu^{2+} -center in KNN X-band EPR is already sufficient to resolve different spectral features, because the EPR line width is drastically reduced (*cf.* Fig. 2(b)). In particular the low-field region of the spectrum, being characteristic for the g_{zz} -orientation, is well resolved. Clearly, two different quartet patterns due to the hyperfine interaction with the copper nuclear spin $I = \frac{3}{2}$ giving $(2I + 1)$, *i.e.* four hyperfine components $A_{\parallel}^{\text{Cu}}$ are observed. The corresponding g_{zz} -value is taken as the center of mass between the second and third hyperfine feature. The two different Cu^{2+} -centers are marked by two stick-spectra. The high-field part of the spectrum is governed by overlapping transitions of different orientations originating from strong copper hyperfine splittings and are further complicated by extra absorption peaks.⁴⁴ In this region, the hyperfine structure is buried under the EPR line width, and the corresponding g -values may be only roughly estimated.

Multi-pulse EPR

Whereas the high-field EPR analysis to first order delivers information on the first coordination sphere about the copper functional center, HYSORE may be employed to considerably enhance the spectral resolution by resolving hyperfine interactions that are buried under the anisotropically-broadened EPR line width. These typically correspond to remote coordination spheres, provided magnetically active nuclei are present. In case of PZT, this mainly holds for the ^{207}Pb -isotope.^{17,34}

The HYSORE spectrum for Cu^{2+} -doped PZT 54/46 is shown in Fig. 4(a).³⁴ It exclusively consists of signals from ^{207}Pb . The $(+, +)$ -quadrant is dominated by a ridge centered at 2.69 MHz, with a width of 3.6 MHz perpendicular to the diagonal. The center position corresponds to the ^{207}Pb -Larmor frequency, giving the identity of the nucleus. The maximum frequency shift $\Delta\nu_s = 90$ kHz along the diagonal is determined by the dipolar component $A_{\parallel}^{\text{Pb}}$ (*cf.* eqn (6)), while the extent of the ridge perpendicular to the diagonal is determined by the distribution of isotropic hyperfine coupling constants a_{iso} . From the observed value of $\Delta\nu_s$ the dipolar hyperfine coupling constant $A_{\parallel}^{\text{Pb}}$ can be estimated⁴⁵ as $A_{\parallel}^{\text{Pb}} = \frac{4}{3}(2\nu_l \Delta\nu_s)^{\frac{1}{2}} = 0.9$ MHz. Additionally, there is a superimposed broad diagonal peak at the spectral region of

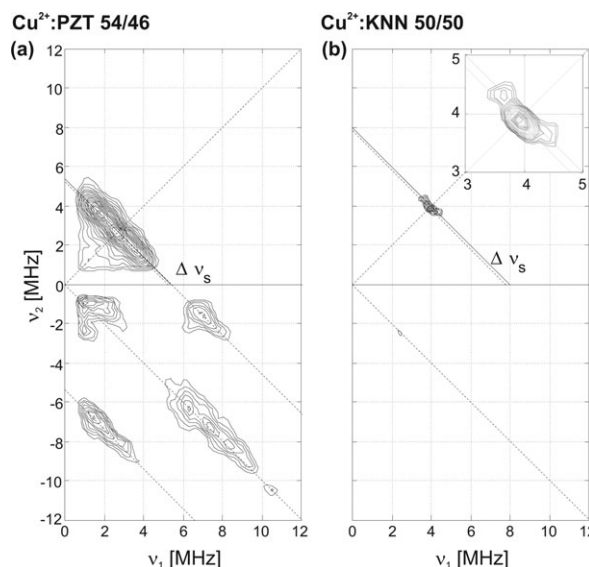


Fig. 4 X-Band HYSORE spectra recorded at 10 K. (a) ^{207}Pb -HYSORE of 0.25 mol%-doped Cu:PZT 54/46.³⁴ (b) ^{23}Na -HYSORE of 0.25 mol%-doped Cu:KNN 50/50.

the ^{207}Pb -Larmor frequency due to contributions from weakly coupled distant ^{207}Pb -nuclei.

In the $(+, -)$ -quadrant, signals extend from $(-1.0, 6.3)$ MHz to $(-3.3, 8.6)$ MHz and from $(-6.3, 1.0)$ MHz to $(-8.6, 3.3)$ MHz. In this case, the dipolar hyperfine interaction spreads the cross-peak ridges parallel to the $-\nu_1 = \nu_2$ diagonal axis, giving $|A_{\parallel}^{\text{Pb}}| = 11.9$ MHz and $|A_{\perp}^{\text{Pb}}| = 7.3$ MHz. The trace of these values amounts to 4.6 MHz, defining the isotropic hyperfine component of these local nuclei to $|a_{\text{iso}}^{\text{Pb}}| = \frac{1}{3}(|A_{\parallel}^{\text{Pb}}| + 2|A_{\perp}^{\text{Pb}}|) = 8.8$ MHz and for the dipolar hyperfine component $|A_{\parallel}^{\text{Pb}}| = \frac{1}{3}||A_{\parallel}^{\text{Pb}}| - |A_{\perp}^{\text{Pb}}|| = 1.5$ MHz. The remaining features along the diagonal in the experimental HYSORE spectra are a result of incomplete inversion of the electron spin echo by the mixing π -pulse.

In Fig. 4(b), the HYSORE spectrum for Cu^{2+} -doped KNN is shown. Obviously, the situation is much different from PZT as a correlation pattern is only observed for the $(+, +)$ -quadrant. The diagonal peak at 3.95 MHz corresponds to the ^{23}Na -Larmor frequency. The maximum frequency shift $\Delta\nu_s$ is determined to 100 kHz and the isotropic ^{23}Na -hyperfine splitting to 1.4 MHz. Concerning the width of the correlation peaks, a similar trend as in the c.w. EPR spectra is observed; for Cu^{2+} :KNN the spectral resolution is considerably enhanced owing to reduced peak width.

Discussion

The accurately determined spin-Hamiltonian parameters will now be transferred into structural information, focusing on two main features at the MPB—local variations in polarization and covalent bonding as induced by the Cu^{2+} -functional center.

For both compounds, Cu^{2+} :PZT 54/46 and Cu^{2+} :KNN 50/50, the ordering of the observed g -values ($g_{\parallel}, g_{zz} > g_{\perp}, g_{xx}, g_{yy}$) is characteristic for octahedrally coordinated Cu^{2+} centers, where the octahedron is elongated by a tetragonal distortion

along the z -axis.³⁸ It can be explained in terms of a five-fold orbital degeneracy of the $3d^9$ ion that is split in the presence of an octahedral crystal field into a triplet (t_{2g}) and a doublet (e_g), with the latter lying lowest. A tetragonal distortion, caused by the crystal field and the Jahn–Teller effect, splits the e_g levels further, resulting in an orbital-singlet $d_{x^2-y^2}$ ground state. Apparently, copper is incorporated at the octahedrally coordinated [Zr,Ti] and Nb-sites, thus acting as an acceptor. The similarity of effective ionic radii between $r_{Ti^{4+}} = 68$ pm, $r_{Zr^{4+}} = 81$ pm, $r_{Nb^{5+}} = 64$ pm and $r_{Cu^{2+}} = 72$ pm as compared to $r_{Pb^{2+}} = 124$ pm, $r_{K^+} = 164$ pm and $r_{Na^+} = 139$ pm supports this assignment.

Furthermore, with respect to the local copper environment the results obtained for Cu^{2+} :PZT give evidence of an intrinsically heterogeneous compound, considering the determined site symmetries for the three different copper centers (*cf.* Fig. 3). This is analogous to the situation in Fe^{3+} -doped PZT, where a defect dipole in the tetragonal phase manifests in EPR signals of two different symmetries as a function of defect-dipole orientation with respect to the orientation of the spontaneous polarization.⁴⁶ The situation for Cu^{2+} -doped PZT is schematically illustrated in Fig. 5(a,b). The third center is due to a defect dipole in the rhombohedral phase (*cf.* Fig. 5(c)). On the other hand, the situation for Cu^{2+} :KNN so far shows only two centers of similar site symmetry but different defect association in terms of one or two associated oxygen vacancies. Consequently, in contrast to Cu^{2+} :PZT 54/46 a rather homogeneous Cu^{2+} :KNN 50/50 material is obtained. High-field EPR will be employed to test this assignment.

With respect to the formation of defect dipoles and their interplay with the direction of spontaneous polarization, a schematic representation is illustrated in Fig. 5. The one kind of defect dipole, $(Cu_{Zr,Ti}^{II} - V_{O}^{\bullet\bullet})^{\times}$ or $(Cu_{Nb}^{III} - V_{O}^{\bullet\bullet})'$, is (partially)

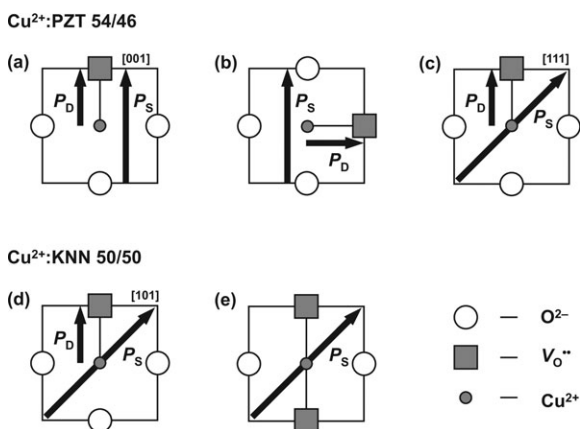


Fig. 5 Schematic representation of defect structure for the pseudo-cubic unit cells for Cu^{2+} -doped PZT (a–c) and Cu^{2+} -doped KNN (d–e), illustrating the interplay between spontaneous polarization and defect dipole. The directions of spontaneous polarization (P_s) along the [001]-orientation for tetragonal phase and along [111] for the rhombohedral (PZT 54/46) and [101] for the orthorhombic (KNN 50/50) phases are indicated. The polarizations for $(Cu_{Zr,Ti}^{II} - V_{O}^{\bullet\bullet})^{\times}$ in PZT (a–c) and $(Cu_{Nb}^{III} - V_{O}^{\bullet\bullet})'$ in KNN (d) are given by P_D . The polarization owing to the electric dipole character for $(V_{O}^{\bullet\bullet} - Cu_{Nb}^{III} - V_{O}^{\bullet\bullet})'$ in KNN is assumed to vanish.

charge compensated by one oxygen vacancy. Consequently, this defect associate contains an *electric dipole* moment $p_D = q \cdot l$ with $q = +2e$ at the oxygen vacancy site and $q = -2e$ ($q = -3e$) at the Cu^{2+} site, both having a distance of about half a lattice constant.^{19,47} The other defect complex that is only present in Cu^{2+} :KNN,²⁸ $(V_{O}^{\bullet\bullet} - Cu_{Nb}^{III} - V_{O}^{\bullet\bullet})'$, is electrically overcompensated with two oxygen vacancies. Tentatively, we expect the two oxygen vacancies coordinated at the two apical sites of the oxygen octahedron. Analogous to the situation reported for acceptor centers in other ferroelectric materials the Cu^{2+} -ion should relax back into the plane spanned by the four equatorial oxygens.^{17,25,48} As a consequence, the distance to the two oxygen vacancies are approximately equal, and the electric dipole moment for that defect associate almost vanishes. On the other hand, both the two $V_{O}^{\bullet\bullet}$ and to somewhat less extent the Cu^{2+} will deform the lattice, which may be described in terms of an *elastic dipole* moment.⁴⁹

Considering the interplay between the present defect associates and structural features of the MPB, the current understanding of the enhanced electro-mechanical response at the MPB is due to an improved ability to ‘rotate’ the direction of spontaneous polarization. This enhanced poling efficiency was first suggested being due to the coexistence of tetragonal and rhombohedral or monoclinic phases.^{51–54} In particular, the availability of fourteen possible domain configurations (six for the tetragonal and eight for the rhombohedral phase) in a *phase-coexistence model* improves the alignment of polar direction in poled ceramic compounds.⁵⁵ An alternative scenario is proposed by the formation of a *nano-scale domain structure*,^{56,57} after which an improved poling efficiency is owing to a miniaturization of the average domain structure. Generally, defect dipoles of the form illustrated in Fig. 5(a–e) tend to increase the overall polarization as to the spontaneous polarization a defect polarization is added.²⁷ On the other hand, for Cu^{2+} :KNN a considerable part of the defect dipoles have a vanishing defect polarization (*cf.* Fig. 5(e)) and thus do not participate to this mechanism. Contrary, the elastic dipoles rather impact the mechanical materials properties explaining the reported enhanced mechanical quality factors for CuO-doped KNN compounds^{58–60} on an atomic scale.

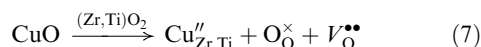
With respect to the observed, relatively broad EPR line widths for Cu^{2+} :PZT, a considerable distribution of spin-Hamiltonian parameters (strain) has to be assumed.⁶¹ Strain is generally due to variations of the local field around the Cu^{2+} -ion and may be particularly pronounced if the ion is preferentially located at grain boundaries, or if there are random electric fields or charge distributions in the ferroelectric material itself. Taking into account the results from ²⁰⁷Pb-HYSCORE, the location at grain boundaries can be excluded. Fast spin relaxation is ruled out as a source of line broadening, since otherwise pulsed EPR experiments would not have been possible. On the other hand, local charge distributions owing to a varying ionicity of the $Cu_{[Zr,Ti]}^{2+}O^{2-}$ bonds in the octahedron, depending on Zr^{4+} or Ti^{4+} being the next nearest neighbor ions,^{62–66} are a source of g - and A^{Cu} -strain. Concerning the microscopic structure of the MPB for PZT, in the model of *mesoscopic phase coexistence* a

distinct set of axial and rhombic (monoclinic) EPR spectra would be expected. In this model, there is no reason for a broad distribution of crystal structures and resulting g -values. Comparing the observed distribution of g -values in relation to the margin set by the distinct g -values of the pure compounds,⁵⁰ additionally *nanoscale composition changes* have to be present. Thus, on top of the phase coexistence model, features occurring on a considerably reduced scale have to be taken into account.

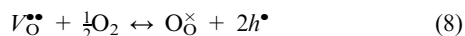
The markedly reduced strain for Cu^{2+} :KNN points to a less pronounced variation of covalent and ionic bonding over the MPB for KNN. Furthermore, as for purely Cu^{2+} -doped KNN there is no need of any rotation of polarization over the MPB, the distribution in possible orientations of defect polarization with respect to spontaneous polarization is considerably confined. However, by lowering the tetragonal-to-orthorhombic phase transition to ambient temperature enhanced dielectric and piezoelectric properties may be achieved.^{10,11,67,68}

The EPR results indicate that the Cu^{2+} primarily, and probably exclusively, occupies the B-site normally occupied by a mixture of Ti^{4+} and Zr^{4+} in PZT, and by Nb^{5+} in KNN. Thus, the dopant oxide, CuO, brings less oxygen per cation into the structure than the binary constituent oxide it replaces, $(\text{Zr,Ti})\text{O}_2$ in PZT and Nb_2O_5 in KNN. It is thus an acceptor dopant that is charge-compensated by oxygen vacancies in the stoichiometric solid solutions that are made up of combinations of stoichiometric binary oxides, as in $\text{Pb}[\text{Zr,Ti}]_{1-z}\text{Cu}_z\text{O}_{3-z}$, or $[\text{K,Na}]\text{Nb}_{1-z}\text{Cu}_z\text{O}_{3-3/2z}$.⁶⁹

The incorporation of CuO into PZT can be written as

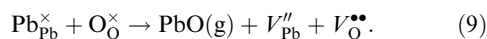


where it is understood that the dopant oxide on the left side is substituted for the host oxide shown above the arrow. This represents the case where no defect complexes form at the high temperatures used for processing or equilibration. There is always the possibility that, because of the presence of unoccupied oxygen sites, that the system will pick up oxygen from the ambient atmosphere with the formation of the charge equivalent of holes.



In fact, PZT is a p-type conductor at high temperatures when measured in high oxygen activities.⁷⁰ However, it has been shown that the extent of oxidation according to eqn (8) does not significantly reduce the concentration of extrinsic oxygen vacancies that result from the acceptor doping.⁷⁰ This to be expected in oxides that contain no oxidizable cations, since a hole is the chemical equivalent of an oxidized cation.

It is well-known that Pb-containing perovskites tolerate Pb-deficiencies up to several percent.⁷¹ This can be viewed as the loss of PbO during processing at high temperatures

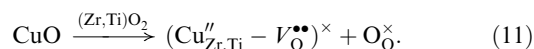


Thus there will be an oxygen vacancy for each Pb vacancy, plus one oxygen vacancy for each doubly charged $\text{Cu}_{\text{Zr,Ti}}''$.

This combination defines the approximation to bulk charge neutrality

$$[V_{\text{O}}^{\bullet\bullet}] \approx [V_{\text{Pb}}''] + [\text{Cu}_{\text{Zr,Ti}}''] \quad (10)$$

Thus, regardless of the amount of Pb-deficiency, there will be enough oxygen vacancies to form the proposed defect complex at lower temperatures. The V_{Pb}'' centers are ‘‘EPR-silent’’, so the EPR results give information only on the environment around the Cu^{2+} ions. The EPR evidence shows extensive formation of the dimer complex $(\text{Cu}_{\text{Zr,Ti}}'' - V_{\text{O}}^{\bullet\bullet})^{\times}$ at low temperatures. The ultimate result of the acceptor doping then is better described as



The complex, being electrically neutral, does not appear in the approximation to bulk charge neutrality, eqn (10).

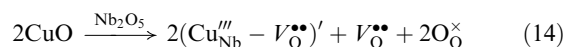
In contrast to PZT, there is no evidence for extensive A-site occupational deficiency in KNN, so the major charged defects should be the Cu^{2+} centers and their charge-compensating lattice defects. EPR shows that Cu^{2+} primarily occupies the B-sites that are normally occupied by Nb^{5+} . The incorporation reaction can then be given as



In this case there are 3/2 oxygen vacancies per Cu center, rather than the 1:1 ratio in PZT. If there is no formation of defect complexes, the approximate expression for bulk charge neutrality would then be

$$2[V_{\text{O}}^{\bullet\bullet}] \approx 3[\text{Cu}_{\text{Nb}}'''] \quad (13)$$

If the defects combine mostly into the complex dimer $(\text{Cu}_{\text{Nb}}''' - V_{\text{O}}^{\bullet\bullet})'$, the ultimate result of the Cu doping can be given by

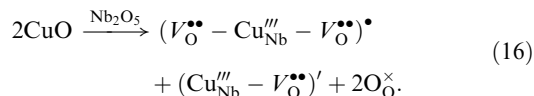


and charge neutrality will be established by

$$2[V_{\text{O}}^{\bullet\bullet}] \approx [(\text{Cu}_{\text{Nb}}''' - V_{\text{O}}^{\bullet\bullet})'] \quad (15)$$

In this case, there will be free $V_{\text{O}}^{\bullet\bullet}$ left over even after all Cu centers have been incorporated into the dimeric complex.

If the Cu is almost all in the form of the dimeric and trimeric complexes, the net result of doping with CuO can be written as



This would ultimately lead to equal concentrations of dimers and trimers. Charge neutrality can be expressed as

$$[(V_{\text{O}}^{\bullet\bullet} - \text{Cu}_{\text{Nb}}''' - V_{\text{O}}^{\bullet\bullet})^{\bullet}] \approx [(\text{Cu}_{\text{Nb}}''' - V_{\text{O}}^{\bullet\bullet})'] \quad (17)$$

The real situation is most likely a mixture of eqn (14),(15) and (16),(17).

Concerning the obtained HYSORE data, in a first attempt the isotropic and orientation-independent nature of the ²⁰⁷Pb-hyperfine interaction has been attributed to the existence

of rather ‘isolated’ $\text{Cu}_{\text{Zr,Ti}}^{\text{II}}$ -centers with the charge-compensating $V_{\text{O}}^{\bullet\bullet}$ being located in distant coordination spheres.³⁴ However, recent DFT calculations for Cu^{2+} -doped PbTiO_3 have shown that the association of the Cu^{2+} -functional center to an $V_{\text{O}}^{\bullet\bullet}$ facilitates the observed isotropic situation as the copper relaxes back into the pseudo-cubic position.¹⁷ When analyzing the determined isotropic ^{207}Pb and ^{23}Na -hyperfine couplings in terms of transferred spin density, a means for sensitively probing the degree of covalent chemical bonding is provided. In this respect, PZT and KNN have in common the general isotropic nature of hyperfine couplings. However, the observed peak widths strongly differ. In case of PZT, this may be explained by a strong variation in nature of chemical bonding. Whereas in PbTiO_3 strong covalent bonding is observed,^{62–65} PbZrO_3 has more ionic bonding.^{65,66} To the contrary, no such variation has been reported for KNN, where covalent bonding is formed on the $\text{Nb}^{5+}\text{-O}^{2-}$ bond whereas the Na^+ and K^+ are ionic in the entire composition range.⁷² When comparing the extent of transferred spin density to the A-site ions in PZT and KNN, taking into account the magnetic moments $\mu^{207\text{Pb}} = 1.00906$ and $\mu^{23\text{Na}} = 2.8629811$, a considerably reduced covalent bonding to the A-site ion is observed in case of Cu^{2+} :KNN.

Conclusion

In summary, structural differences in the copper functional center site in 0.25 mol% Cu^{2+} -doped $\text{Pb}[\text{Zr}_{0.54}\text{Ti}_{0.46}]\text{O}_3$ (PZT) and $[\text{K}_{0.5}\text{Na}_{0.5}]\text{NbO}_3$ (KNN) ferroelectrics have been characterized by means of multi-frequency and multi-pulse EPR spectroscopy. The results obtained suggest that Cu^{2+} substitutes for both systems as an acceptor centre for the perovskite B-site. For reasons of local charge compensation different kinds of defect complexes involving one and two oxygen vacancies are formed. These differ in their electric and elastic properties. The results obtained are analyzed in order to characterize differences in the nature of the morphotropic phase boundary between the two systems. In particular, it is found that Cu^{2+} -doping in KNN creates more oxygen vacancies than the same amount of copper in PZT. Furthermore, local differences in the nature of chemical bonding are monitored.

Acknowledgements

This research has been financially supported by the DFG through project EI 498/1-1 and the centre of excellence 595 ‘Electrical Fatigue in Functional Materials’. The continuous support of Prof. Stefan Weber is greatly acknowledged.

References

- 1 B. Jaffe, W. R. Cook and H. Jaffe, *Piezoelectric Ceramics*, Academic Press, 1971.
- 2 Y. Xu, *Ferroelectric Materials and their Applications*, Elsevier, Amsterdam, 1991.
- 3 M. E. Lines and A. M. Glass, *Principles and Applications of Ferroelectrics and Related Materials*, Oxford University Press, Oxford, 2001.
- 4 A. J. Moulson and J. M. Herbert, *Electroceramics – Materials, Properties, Applications*, Wiley, Chichester, 2003.

- 5 R.-A. Eichel, *J. Electroceram.*, 2007, **19**, 9–21.
- 6 R.-A. Eichel, *J. Am. Ceram. Soc.*, 2008, **91**, 691–701.
- 7 C. Elissalde and J. Ravez, *J. Mater. Chem.*, 2001, **11**, 1957–1967.
- 8 M. J. Hoffmann and H. Kungl, *Curr. Opin. Solid State Mater. Sci.*, 2004, **8**, 51.
- 9 Y. Saito, H. Takao, T. Tani, T. Nonoyama, K. Takatori, T. Homma, T. Nagaya and M. Nakamura, *Nature*, 2004, **432**, 84–87.
- 10 Y. Guo, K. Kakimoto and H. Ohsato, *Appl. Phys. Lett.*, 2004, **85**, 4121.
- 11 E. Hollenstein, M. Davis, D. Damjanovic and N. Setter, *Appl. Phys. Lett.*, 2005, **87**, 182905.
- 12 H. Fu and R. E. Cohen, *Nature*, 2000, **403**, 281.
- 13 B. Noheda, D. E. Cox, G. Shirane, S. E. Park, L. E. Cross and Z. Zhong, *Phys. Rev. Lett.*, 2001, **86**, 3891.
- 14 L. Bellaiche, A. Garcia and D. Vanderbilt, *Phys. Rev. B: Condens. Matter Mater. Phys.*, 2001, **64**, 060103.
- 15 L. Wu, J. L. Zhang, C. L. Wang and J. C. Li, *J. Appl. Phys.*, 2008, **103**, 084116.
- 16 Y. J. Dai, X. W. Zhang and P. K. Chen, *Appl. Phys. Lett.*, 2009, **94**, 042905.
- 17 R.-A. Eichel, P. Erhart, P. Träskelin, K. Albe, H. Kungl and M. J. Hoffmann, *Phys. Rev. Lett.*, 2008, **100**, 095504.
- 18 H. Neumann and G. Arlt, *Ferroelectrics*, 1987, **76**, 303.
- 19 G. Arlt and H. Neumann, *Ferroelectrics*, 1988, **87**, 109.
- 20 E. Siegel and K. A. Müller, *Phys. Rev. B: Condens. Matter Mater. Phys.*, 1979, **19**, 109.
- 21 E. Siegel and K. A. Müller, *Phys. Rev. B: Condens. Matter Mater. Phys.*, 1979, **20**, 3587.
- 22 W. L. Warren, G. E. Pike, K. Vanheusden, D. Dimos, B. A. Tuttle and J. Robertson, *J. Appl. Phys.*, 1996, **79**, 9250.
- 23 W. L. Warren, B. A. Tuttle, F. C. Rong, G. J. Gerardi and E. H. Poindexter, *J. Am. Ceram. Soc.*, 1997, **80**, 680.
- 24 R. Merkle and J. Maier, *Phys. Chem. Phys.*, 2003, **5**, 2297.
- 25 H. Meštrić, R.-A. Eichel, T. Kloss, K.-P. Dinse, So. Laubach, St. Laubach and P. C. Schmidt, *Phys. Rev. B: Condens. Matter Mater. Phys.*, 2005, **71**, 134109.
- 26 H. Meštrić, R.-A. Eichel, K.-P. Dinse, A. Ozarowski, J. van Tol, L. C. Brunel, H. Kungl, M. J. Hoffmann, K. A. Schöna, M. Knapp and Hartmut Fuess, *Phys. Rev. B: Condens. Matter Mater. Phys.*, 2006, **73**, 184105.
- 27 L. X. Zhang, E. Erdem, X. Ren and R.-A. Eichel, *Appl. Phys. Lett.*, 2008, **93**, 202901.
- 28 E. Erüna, S. Körbel, C. Elsässer, J. Acker, H. Kungl, M. J. Hoffmann and R.-A. Eichel, submitted.
- 29 R.-A. Eichel, H. Meštrić, H. Kungl and M. J. Hoffmann, *Appl. Phys. Lett.*, 2006, **88**, 122506.
- 30 R. Böttcher, C. Klimm, D. Michel, H.-C. Semmelhack, G. Völkel, H.-J. Gläsel and E. Hartmann, *Phys. Rev. B: Condens. Matter Mater. Phys.*, 2000, **62**, 2085.
- 31 H. Meštrić, R.-A. Eichel, K.-P. Dinse, A. Ozarowski, J. van Tol and L. C. Brunel, *J. Appl. Phys.*, 2004, **96**, 7440–7444.
- 32 E. Erdem, R. Böttcher, H. J. Gläsel and E. Hartmann, *Magn. Reson. Chem.*, 2005, **43**, 174–182.
- 33 R.-A. Eichel, K.-P. Dinse, H. Kungl, M. J. Hoffmann, A. Ozarowski, J. van Tol and L. C. Brunel, *Appl. Phys. A: Mater. Sci. Process.*, 2005, **80**, 51.
- 34 R.-A. Eichel, H. Kungl and M. J. Hoffmann, *J. Appl. Phys.*, 2004, **95**, 8092–8096.
- 35 R. Böttcher, W. Brunner, B. Milsch, G. Völkel, W. Windsch and S. T. Kirillov, *Chem. Phys. Lett.*, 1986, **129**, 546.
- 36 R.-A. Eichel, M. D. Drahus, P. Jakes, E. Erüna, E. Erdem, S. K. S. Parashar, H. Kungl and M. J. Hoffmann, *Mol. Phys.*, DOI: 10.1080/00268970903084920, in press.
- 37 P. Erhart, R.-A. Eichel, P. Träskelin and K. Albe, *Phys. Rev. B: Condens. Matter Mater. Phys.*, 2007, **76**, 174116.
- 38 A. Abragam and B. Bleaney, *Electron Paramagnetic Resonance of Transition Ions*, Clarendon Press, Oxford, 1970.
- 39 Hyperfine interactions with other nuclei present in the PZT and KNN materials, such as ^{91}Zr , $^{47,49}\text{Ti}$, ^{39}K , $^{143,145}\text{Nb}$ or ^{17}O , were not resolved in the HYSORE spectra and thus are neglected.
- 40 J. van Tol, L. C. Brunel and R. J. Wylde, *Rev. Sci. Instrum.*, 2005, **76**, 074101.
- 41 P. Höfer, A. Grupp, H. Nebenführ and M. Mehring, *Chem. Phys. Lett.*, 1986, **132**, 279.

- 42 C. Gemperle, G. Aebli, A. Schweiger and R. R. Ernst, *J. Magn. Reson.*, 1990, **88**, 241.
- 43 S. Stoll and A. Schweiger, *J. Magn. Reson.*, 2006, **178**, 42–55.
- 44 R.-A. Eichel and A. Schweiger, *J. Magn. Reson.*, 2001, **152**, 276–287.
- 45 A. Pöppel and L. Kevan, *J. Phys. Chem.*, 1996, **100**, 3387.
- 46 E. Erdem, R.-A. Eichel, H. Kungl, M. J. Hoffmann, A. Ozarowski, J. van Tol and L. C. Brunel, *Phys. Scr.*, 2007, **T129**, 12–16.
- 47 P. V. Lambeck and G. H. Jonker, *Ferroelectrics*, 1978, **22**, 729.
- 48 K. A. Müller, W. Berlinger and J. Albers, *Phys. Rev. B: Condens. Matter Mater. Phys.*, 1985, **32**, 5837.
- 49 A. S. Nowick and B. S. Berry, *Anelastic Relaxation in Crystalline Solids*, Academic Press, New York, 1972.
- 50 R.-A. Eichel, H. Meštrić, K. P. Dinse, A. Ozarowski, J. van Tol, L. C. Brunel, H. Kungl and M. J. Hoffmann, *Magn. Reson. Chem.*, 2005, **43**, S166–S173.
- 51 P. Ari-Gur and L. Benguigui, *J. Phys. D: Appl. Phys.*, 1975, **8**, 1856.
- 52 W. Cao and L. E. Cross, *Phys. Rev. B: Condens. Matter Mater. Phys.*, 1993, **47**, 4825.
- 53 R. Ragini, R. Ranjan, S. K. Mishra and D. Pandey, *J. Appl. Phys.*, 2002, **92**, 3266.
- 54 J. Frantti, S. Ivanov, S. Eriksson, H. Rundlöf, V. Lantto, J. Lappalainen and M. Kakihana, *Phys. Rev. B: Condens. Matter Mater. Phys.*, 2002, **66**, 064108.
- 55 V. A. Isupov, *Solid State Commun.*, 1975, **17**, 1331.
- 56 K. A. Schönau, L. A. Schmitt, M. Knapp, H. Fuess, R.-A. Eichel, H. Kungl and M. J. Hoffmann, *Phys. Rev. B: Condens. Matter Mater. Phys.*, 2007, **75**, 184117.
- 57 W. F. Rao and Y. U. Wang, *Appl. Phys. Lett.*, 2007, **91**, 052901.
- 58 E. Li, H. Kakemoto, S. Wada and T. Tsurumi, *J. Am. Ceram. Soc.*, 2007, **90**, 1787–1791.
- 59 E. Li, H. Kakemoto, S. Wada and T. Tsurumi, *IEEE Trans. Ultrason. Ferroelectron. Freq. Control*, 2008, **55**, 980–987.
- 60 N. Marandian Hagha, K. Kermana, B. Jadidianb and A. Safaria, *J. Eur. Ceram. Soc.*, 2009, **29**, 2325–2332.
- 61 W. Froncisz and J. S. Hyde, *J. Chem. Phys.*, 1980, **73**, 3123–3131.
- 62 R. E. Cohen, *Nature*, 1992, **358**, 136–138.
- 63 H. Miyazawa, E. Natori, S. Miyashita, T. Shimoda, F. Ishii and T. Oguchi, *Jpn. J. Appl. Phys.*, 2000, **39**, 5679–5682.
- 64 Y. Kuroiwa, S. Aoyagi, A. Sawada, J. Harada, E. Nishibori, M. Takata and M. Sakata, *Phys. Rev. Lett.*, 2001, **87**, 217601.
- 65 G. A. Rossetti, *Br. Ceram. Trans.*, 2004, **103**, 83–87.
- 66 S. Aoyagi, Y. Kuroiwa, A. Sawada, H. Tanaka, J. Harada, E. Nishibori, M. Takata and M. Sakata, *J. Phys. Soc. Jpn.*, 2002, **71**, 2353–2356.
- 67 R. Wang, R. J. Xie, K. Hanada, K. Matsuaki, H. Bando, T. Sekiya and M. Itoh, *Ferroelectrics*, 2006, **336**, 39–46.
- 68 Y. Saito and H. Takao, *Ferroelectrics*, 2006, **338**, 17–32.
- 69 D. M. Smyth, *The Defect Chemistry of Oxides*, Oxford University Press, New York, 2000, ch. 5.
- 70 M. V. Raymond and D. M. Smyth, *Ferroelectronics*, 1993, **144**, 433.
- 71 R. L. Holman and R. M. Fulrath, *J. Appl. Phys.*, 1973, **44**, 5227.
- 72 C. Moriyoshi, J. Kato, Y. Terado, S. Wada, M. Takata and Y. Kuroiwa, *Jpn. J. Appl. Phys.*, 2008, **47**, 7745–7748.